Additive manufacturing of highly reconfigurable plasmonic circuits for terahertz communications

Yang Cao, Kathirvel Nallappan, Hichem Guerboukha, Guofu Xu, and Maksim Skorobogatiy

Abstract: Terahertz communications is a booming field in rapid development. While in most of the existing terahertz communication systems, modulated THz carrier wave is transmitted via free-space communication channels, the THz waveguide-based integrated solutions can be of great utility both at the transmitter and receiver ends. Thus, at the transmitter end they can be used for steering, beam forming, and multiplexing of the THz signals. At the receiver end, terahertz waveguide-based solutions can be used as reliable interconnects (especially in the geometrically complex environments, ex. intra-vehicle communications), as well as for real-time analogue signal processing such as filtering and demultiplexing. More generally, waveguide-based THz optical circuits are indispensable for miniaturization and mass production of cost-effective THz communication systems. In this work, we present comprehensive numerical, fabrication and optical characterization studies of a new type of modular THz integrated circuits based on the micro-encapsulated two-wire plasmonic waveguides. Particular attention is payed to the design of optimized components such as waveguides, couplers and waveguide Bragg gratings to realize easy to handle, highly reconfigurable terahertz circuits capable of complex functionalities such as multiplexing and demultiplexing. The basic element of all the developed subcomponents is a low-loss low-dispersion two-wire waveguide suspended inside of a protective micro-sized enclosure (cage) using deeply subwavelength dielectric supports. The high resolution stereolithography 3D printing and wet chemistry metal deposition techniques are employed to fabricate such waveguides where the THz light is mainly confined in the air gap between the two wires. First, the straight waveguides are characterized using continuous-wave THz spectroscopy system with the measured transmission loss and group velocity dispersion (GVD) of 6 m^{-1} and -1.5 ps/THz·cm respectively at the carrier frequency of 140 GHz. Next, waveguide bends and a Y-coupler based on the two coalescing waveguide bends are studied. We find that due to the presence of a cage, the curved two-wire waveguides show smaller bending loss than the free-standing two-wire waveguides of similar geometry. Additionally, we find that relatively tight bends of ~5cm-radius can be well tolerated by adding less than ~10 m^{-1} propagation losses to the curved waveguide propagation loss. Next, we design and fabricate the two-wire waveguide Bragg gratings by hot stamping a periodic sequence of metal strips onto a paper sheet and inserting it into the air gap between the two-wire waveguides. The geometry of the grating featuring a Bragg frequency of 140 GHz is studied theoretically and numerically, and the optimal waveguide gratings are then realized experimentally. Such structures can have bandwidths as high as ~20 GHz. Finally, using thus developed modular components, a two channel THz Add-Drop Multiplexer (ADM) is demonstrated for the operation at 140 GHz carrier frequency and featuring a spectral width of 2.8 GHz. We believe that the reported modular platform based on the micro-encapsulated two-wire waveguides can have a strong impact on the field of integrated optical circuits for THz signal processing and potentially sensing due to ease of device fabrication (standard 3D printers and wet chemistry), modular design and high degree of reconfigurability, low-loss and low-dispersion of the underlying waveguides, as well as high potential for the real-time tunability of the optical circuits due to ease of access of the modal fields inside the controlled in-cage environment.

Keywords: Terahertz photonics, plasmonic two-wire waveguides, 3D printing, THz communications, add-drop multiplexers

1. Introduction

The explosive growth of data traffic over past decades has placed increasing demands on the communication systems. With data rates in excess of 100 Gbps, the terahertz (THz) wireless communications is poised to become an enabling technology for the next-generation communications networks [1]. The high directionality and limited propagation range of THz radiation offers enhanced security and resistance to eavesdropping. At the same time, the high directionality of THz radiation poses many challenging engineering problems such as complexity in discovering the THz network (homing to emitter location) [2] , as well as necessity of precise alignment between the transmitter and receiver modules, thus requiring the use of advanced beam steering solutions [3, 4]. While mechanical solutions to beam steering are available in various forms (ex. Galva mirror scanners), a more reliable and robust solution would ideally forgo the use of moving parts and rather employ integrated solutions such as passive and active leaky waveguides and leaky wave antennas [5-8]. In the microwave and THz range such structures often employ metallic waveguides [10,11] as well as modes propagating along conductive surfaces [12-14] (which in THz range are also known as Sommerfeld waves or Zenneck waves depending on the material of a surface). In this respect, development of integrated metallic waveguides supporting various types of plasmonic modes is of great interest. Beyond the use in advanced beam steering and detection, integrated THz optical circuits provide a remarkable technological platform for signal processing in THz communications [15, 16]. Unlike the cumbersome and prone to time drift assemblies of discrete free-space components, the use of integrated circuits improves long term reliability, results in a smaller footprint, and is better suitable for mass production. Therefore, development of THz integrated optical circuits is a promising direction for signal processing at THz frequencies.

One promising low-loss material that was identified for building THz circuits is silicone. Both total internal reflection waveguides and slab photonic crystal-based waveguides were explored to build THz integrated optical circuits [17]. Various optical elements such as ring resonators, filters, and couplers on silicon substrates have been demonstrated in the THz range [18-23]. However, the fabrication of silicon optical circuits generally requires the use of costly top of the line fab infrastructure (lithography systems, deep reactive ion etchers and bonders, etc.) as well as high cost materials (gold, etc.) in a multi-stage fabrication process. Furthermore, high refractive index contrast normally associated with silicone photonics results in challenging fabrication tolerances even for longer THz wavelengths [24]. Finally, silicone integrated photonics is inherently planar, with very limited capacity for 3D integration, and out-of-plane inter-chip connectorization.

Alternatively, the inherently 3D additive manufacturing presents an interesting alternative to the mostly planar silicone photonics. Thus, large-scale THz waveguide-based circuits can be rapidly manufactured with deeply subwavelength precision using readily available low-cost SLA (Stereo Lithography) or FDM (Filament Deposition Modeling) tools. While featuring lower refractive index contract material combinations than silicone photonics, additive manufacturing results in more relaxed fabrication tolerances and less stringent alignment requirements. Owing to the ubiquitous availability of hardware, the low threshold for entering into production, as well as the ease of 3D integration and out-of-plane inter-chip interconnect solutions, additive manufacturing emerges as a promising platform for manufacturing waveguide-based optical integrated circuits in the THz spectral range. One of the challenges for additive manufacturing in THz is the lack of low-loss materials (thermoplastics for FDM and photocurable resins for SLA). In this respect, the search for new materials or novel waveguide designs is of critical importance for 3D printed THz integrated circuits.

Compared to other reported THz waveguides that were developed for THz communication applications, such as subwavelength fibers [3,24,25], porous fibers [26,27], tube-shaped hollow-core waveguides [28-30], and parallel plate waveguides (PPWG) [31,32], the two-wire THz plasmonic waveguides have advantages of low transmission loss, negligible group velocity dispersion (GVD), no cut-off frequency, and high coupling coefficient with the conventional linear-polarized THz sources [33].

Most of the two-wire waveguides that were studied earlier featured short sections of straight metallic wires fixed in bulky holders, were inconvenient to use, and were unsuitable for building integrated circuits. Although handling and mechanical stability of the two-wire waveguides can be improved by embedding them into foams or other types of porous dielectric claddings [33-36], interaction of the modal fields with lossy materials of the cladding results in increased Group Velocity Dispersion (GVD) and transmission losses, thus limiting utility of classic two-wire waveguides in communication applications.

In this paper we develop a novel type of quasi-two-wire waveguides, as well as optical components based on such waveguides using optically thick metal layers deposited onto complex-shaped 3D printed mechanical supports. In fact, the principal goal of this work is to explore THz optical component fabrication using complex metallized 3D shapes that can be readily manufactured using standard Stereo Lithography 3D printers. The idea is to ultimately go out of plane and pursue 3D optical integration of THz components, which is simply impossible using standard lithographic techniques used in the fabrication of most microwave and optical components. Additionally, for sensing applications as well as for the design of highly tunable THz components we want to have access to the modal fields, which is especially simple to achieve when using two-wire waveguides [37,38]. Finally, using 3D printing allows seamless integration between the enabling optical elements (waveguides, resonators, etc.) as well as mechanical support and environmental isolation (protective cage around the waveguide, holders, alignment features and connectors, etc.) that ultimately results in convenient to handle, highly modular systems that are easy to assemble and maintain.

Owing to the relatively high resolution (~25 μm), large build volumes (~15cm x 15cm), superior reproducibility, as well as due to wide availability, low infrastructure and maintenance costs, the SLA 3D printing technique is perfectly suitable for the fabrication of various types of THz components. As a result, considerable amount of 3D printing work has been reported for the fabrication of THz dielectric components [39-42]. At the same time, fabrication of THz plasmonic structures is more subtle and less studied due to necessity of the metallization step that has to produce high quality optically thick films (several 100-300 nm for THz frequencies [43]) on complex-shaped polymer surfaces. Recently, efficient metallization and coating techniques for 3D printed parts were reported using standard sputtering techniques [44], as well as more advanced wet or aerosol chemistries with resulting metallic coatings performing comparably to the components machined from bulk metals [45,46].

In what follows, we present the in-depth theoretical and experimental studies of the 3D printed two-wire THz plasmonic waveguide-based components and modular optical circuits based on such components. Highly reconfigurable nature of the developed THz plasmonic circuits are demonstrated by assembling nontrivial optical components (ex., Add Drop Multiplexer (ADM)) using basic building blocks such as waveguides, bends, Y-splitters and Waveguide Bragg Gratings (WBGs), all based on the encapsulated two-wire plasmonic waveguides.

Our paper is organized as follows. First, we present the fundamental building block of the proposed plasmonic optical circuits – a two-wire waveguide which is encapsulated into a protective micro-sized cage that can be handled directly and that has various self-alignment features. We start with a numerical study and optimization of the optical guidance properties of such waveguides including their loss, GVD, and coupling efficiency to the WR6.5 flange waveguide for the operation frequency of ~140 GHz set by our experimental setup. Then, the two-wire waveguides are fabricated using stereolithography (SLA) 3D printing and wet chemistry deposition techniques, and their performance is experimentally characterized using the Continuous Wave (CW) THz spectroscopy and a cut-back method. Experimentally found waveguide transmission loss and GVD of the straight two-wire waveguide sections were measured as ~6 m^{-1} and -1.5 ps/THz·cm at 140 GHz, respectively. Next, bending losses of the curved two-wire encapsulated waveguides with different bend radiuses and axis of rotation were studied numerically and experimentally. We find that the resin cage significantly reduces bending loss of a two-wire encapsulated waveguide compared to that of a free-standing two-wire waveguide due to modal field enhancement within the cage. We also find that even relatively tight bends with the bending radii of 5 cm result in only modest increase in the modal propagation loss of less than 10 m^{-1}. Next, we explore design and fabrication of paper-based symmetric metal gratings that are made using low-cost hot stamping technique involving a laser jet printer and metallic thermofoils. Resonant transmission properties of such Waveguide Bragg Gratings (WBGs) can be readily explained by the destructive interference between the fundamental mode of a two-wire waveguide and the fundamental mode of a planar metallic waveguide formed by the metallic grating elements. Experimentally measured transmission dips with 25dB suppression factor and spectral widths as large as 32 GHz (FWHM) at 140 GHz were measured with thus designed 5 cm-long, 1.5mm period WBGs. Finally, we present two reconfigurable THz plasmonic circuits as demonstrators for signal processing in the THz transmitter and receiver circuits, including a THz splitter/multiplexer and an Add Drop Multiplexer (ADM) prototype. Thus, at first a Y-shaped splitter/multiplexer was fabricated using a combination of two 90^{o} waveguide bends of 4cm bend radius; in fact, the splitter is assembled using two 45^{o} waveguide bend sections and a Y-coupler element. Experimentally, we find that the splitter introduces a negligible insertion loss (<0.5 dB) and a very small crosstalk (<-20 dB). Finally, we use a WBG in one of the arms of a Y-splitter and demonstrate a two channel ADM with In, Through and Drop ports operating at ~140 GHz and having a spectral width of ~2.8 GHz.

2. Two-wire waveguides

The main difference between the proposed micro-encapsulated and conventional two-wire waveguides is the presence of a dielectric support. Such a support serves several functions such as shielding of the modal field from the influence of environment during handling, while also incorporating various alignment features to simplify system integration of several plasmonic components. Particularly, the resin cage with dielectric supports used for wire encapsulation keeps the two wires parallel to each other, while maintaining the gap between the two with high precision due to high definition of the 3D printing process. Moreover, several mechanical alignment features are integrated into the cage structure to simplify waveguide coupling to the external sources (horn antennas, etc.), as well as between different sections of the plasmonic waveguides or other components. With the proper design, the cage surrounding the two wires has only a small impact on the THz surface plasmon polariton (SPP) wave, which is mainly confined to the air region between the two wires.

The THz rectangular metallic waveguides (waveguide flanges) have been widely used in the THz transmitter and receiver circuits. When developing the two-wire waveguide-based plasmonic circuits for THz communications, we first choose the parameters of a two-wire waveguide to optimise butt-coupling efficiency with a standard WR6.5 waveguide flange (hollow rectangular waveguide with sizes of hzWR6=825.5 μm, hyWR6=1651 μm) used for operation at 140 GHz. Fig. 1. (a) is a schematic of the two waveguides at the coupling plane. To characterise coupling efficiency between the two waveguides, we employ mode matching technique [43, 47, 48] using vectorial fields of the two waveguides computed using the finite element COMSOL Multiphysics. Particularly, assuming that all the incoming power is in the fundamental TE_{10} mode of the WR6.5 waveguide $|F_{in}^{+}\rangle$ with electric field polarized along the shorter side of a waveguide, then ignoring reflections, complex field coupling coefficient C into the fundamental mode of the two-wire waveguide $|F_{out}^{+}\rangle$ can be found using field averages with respect to the longitudinal flux operator $\hat{S}_z$ as:

$$C = \frac{\left\langle F_{out}^{+} \middle| \hat{S}_z \middle| F_{in}^{+} \right\rangle}{\sqrt{\left\langle F_{out}^{+} \middle| \hat{S}_z \middle| F_{out}^{+} \right\rangle \left\langle F_{in}^{+} \middle| \hat{S}_z \middle| F_{in}^{+} \right\rangle}} = \frac{\frac{c}{16\pi} \int\limits_{wc} dxdy (E_{t,out}^{*}(x,y) \times H_{t,in}(x,y) + E_{t,in}(x,y) \times H_{t,out}^{*}(x,y))}{\sqrt{\frac{c}{8\pi} \mathrm{Re} \int\limits_{wc} dxdy (E_{t,out}^{*}(x,y) \times H_{t,out}(x,y)} \cdot \sqrt{\frac{c}{8\pi} \mathrm{Re} \int\limits_{wc} dxdy (E_{t,in}^{*}(x,y) \times H_{t,in}(x,y)}} , \quad [1]$$

where integrals are performed over the whole waveguide crossection plane using transverse modal fields. Note that the modal excitation coefficient (by power) is given by $|C|^2$. In our simulations, the metallic wires are modeled using Impedance Boundary Condition (IBC) at the wire surface together with the Drude-Lorentz model for the dielectric constant ε_m of silver in THz spectral range taken from [49]:

$$\varepsilon_m = 1 - \frac{\omega_p^2}{\omega^2 + i\omega\gamma} \quad [2]$$

where ω_p=2π·2.185e15 Hz is the plasma frequency, and γ_b=2π·0.5138e13 Hz is the damping coefficient for the bulk Ag metal. As explained later in the paper, realistic modeling of plasmonic wave losses at metal surfaces in the THz range requires using much higher values of the dumping coefficient in the Drude-Lorentz model, or using of a different model altogether (ex. Drude-Smith). Therefore, in the rest of the paper in our simulations we use model (2) we use a fitted value of the damping coefficient γ_s =2π·2.69e14 Hz to account for the surface imperfections.

In all the Fig. 1. (b) shows the modal electric field distribution of the THz SPP wave supported by the stand-alone two-wire waveguide. The field is mainly confined to the air gap between the two wires, while extending somewhat in the transverse direction from the wires. To optimise power coupling coefficient between the modes of a WR6.5 waveguide and a two-wire waveguide, we vary the gap size between the wires, as well as the wire diameter. The values of the power coupling coefficient $|C|^2$ and modal losses (by field) are shown in the Figs. 1. (e) and 1. (f) as blue stars. The maximal power coupling coefficient of 45.43% is obtained using wires featuring the diameter of WD=0.4·hyWR6 and the gap size of AG=0.8·hzWR6. Then, using the modal field distribution of the fundamental mode of a bare two-wire waveguide, the geometry of the resin cage encapsulating the wires (see Fig. 1. (c)) was chosen so that the electric field intensity at the internal horizonal and vertical boundaries of a cage do not exceed 3% of the maximal value in the waveguide gap. We then recomputed the plasmonic waveguide losses, as well as the coupling coefficient between the WR6.5 waveguide flange and micro-encapsulated two-wire waveguides to study the effect of the cage on the waveguide modal properties. The corresponding values of the coupling coefficient and modal losses are shown in the Figs. 1. (e) and 1. (f) as red stars. In our numerical simulations, the refractive index of resin used in 3D printing and its losses are taken from the experimental studies presented in Ref [39]. Particularly, at 140 GHz, their values are 1.644 and 0.45 cm^{-1} (by field) respectively.

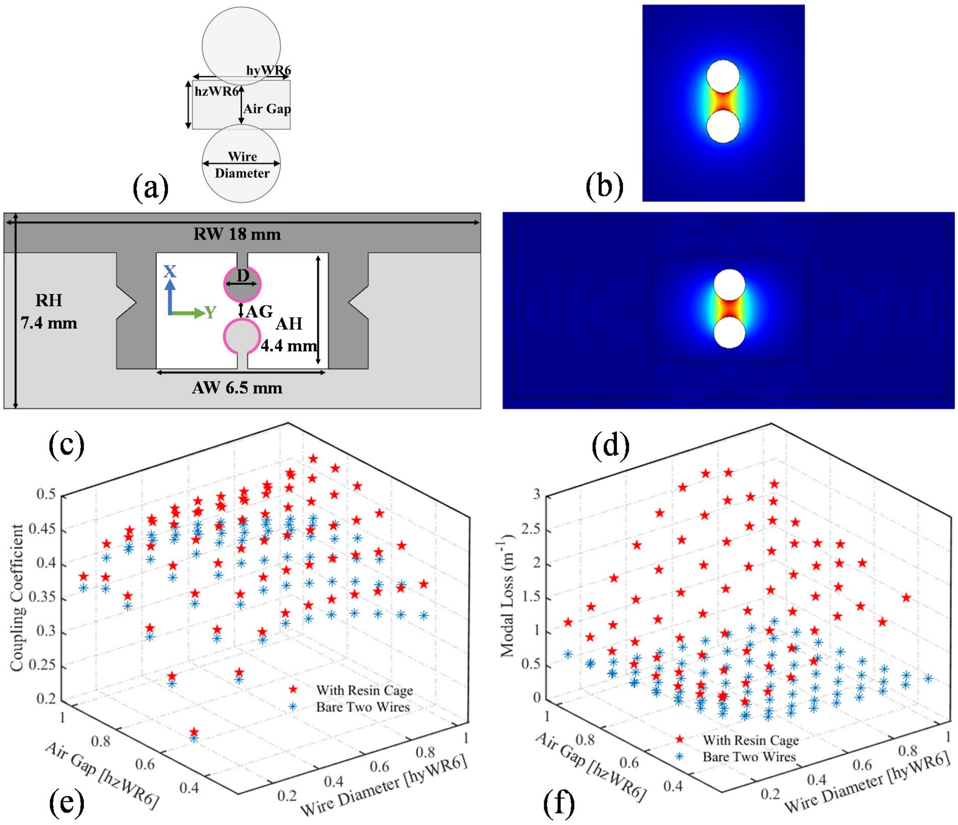

Fig. 1 (a) Schematic of the butt-coupling arrangement between a two-wire waveguide and a WR6.5 waveguide flange. (b) Modal electric field amplitude distribution $|E|$ of the THz SPP wave supported by the stand-alone two-wire waveguide at 140 GHz of $0.8 \cdot$ hyWR6 wire diameter and $0.8 \cdot$ hzWR6 inter-wire separation. (c) Schematic of the micro-encapsulated two-wire waveguide cross section featuring two 3D printed parts (different shades of gray) each featuring a plastic cylinder covered with a silver layer (magenta) that are suspended in air (white) using dielectric supports and encapsulated within a plastic cage (grey). (d) Modal electric field amplitude distribution $|E|$ at 140 GHz for a 3D printed two-wire waveguide with silver layer coated wires placed inside of a resin enclosure. The two-wire waveguide geometry is the same as in Fig. 1. (b), the cage size is the same as indicated in Fig. 1. (c). (e) Dependence of the coupling coefficient (by power) between the fundamental modes of a WR6.5 waveguide flange and a two-wire waveguide (with and without cage) as a function of the wire diameter and inter-wire separation at 140 GHz. (f) Dependence of the fundamental mode propagation loss (by field) of a two-wire waveguide (with and without cage) as a function of the wire diameter and the inter-wire separation at 140 GHz.

By comparing the transverse electric field distributions of the THz SPP waves supported by the two-wire waveguides with and without the resin cage (Figs. 1. (b) and (d)), we note that presence of a resin cage leads to a somewhat tighter confinement of the fundamental mode in the waveguide gap. This, in turn, leads to a somewhat higher power excitation efficiency of the encapsulated waveguide fundamental mode (47.61% as seeing from Fig. 1. (e)) in case of an encapsulated waveguide, while also results in the higher propagation losses of such waveguides due to presence of the modal fields in the lossy material of a cage (see Fig. 1. (f)). Increased modal confinement due to presence of a cage can be explained by "squeezing" of the modal filed in the vertical direction (Z-axis) due to discontinuity of the electric field component at the top and bottom horizonal boundaries between the cage and the air regions. Particularly, at the horizontal boundaries the Z component of the electric field dominates. At such boundaries, the Z displacement field is continuous across the interface, therefore, the dominant Z component of the electric field in the plastic cage of dielectric constant ε_{pl} is going to be smaller than that in the air (with dielectric constant ε_{air}) by the fraction $\varepsilon_{air}/\varepsilon_{pl}$, which forces redistribution of the modal field towards the inside of the cage, hence higher presence of the modal field in the gap between the wires.

Moreover, as seen from Fig. 1. (f) (red stars), when increasing the wire diameter or the inter-wire separation (while keeping cage size the same) modal size also increases, thus leading to increase in the modal propagation losses due to its stronger overlap with the lossy cage material. This is in contrast to the fundamental mode of a stand-alone two-wire waveguide whose modal losses decrease when using larger diameter wires or larger inter-wire separations (See Fig. 1. (f) blue stars), due to the lower presence of the modal fields in the lossy metal material of the wires [50].

As seen from Fig. 1. (e), the two-wire waveguide excitation efficiency is strongly sensitive to the value of the inter-wire separation with an optimal value $AG \approx 0.8 \cdot \mathrm{hzWR6} = 660\ \mu\mathrm{m}$ regardless of the wire diameter. At the same time, excitation efficiency is only weakly sensitive to the wire diameter, as long as it is larger than $WD > 0.4 \cdot \mathrm{hyWR6} = 660\ \mu\mathrm{m}$. From the fabrication point of view, the inter-wire distance is defined by the vertical resolution of the printer and is superior to $25\ \mu\mathrm{m}$

for the stereolithography (SLA) ASIGA 2 printer that we used. At the same time, wire shape is rather defined by the transverse resolution of the printer, which is on the order of $50 - 100$ μm, and thus, fabrication of the larger wire diameters is more reliable. In our experiments we found that we can reliably and consistently manufacture waveguides with the optimal inter-wire separation $0.8 \cdot \text{hzWR6} = 660$ μm, while somewhat larger wire diameters of $WD \approx 0.8 \cdot \text{hyWR6} = 1.32$ mm. As expected, at 140GHz, the resultant waveguide has a high power excitation efficiency of 47.61% with the WR6.5 flange, which is close to that of the theoretical maximal value of 48.16%. Theoretical loss (by field) of a straight waveguide is estimated at ~2.3 m^{-1} which is higher than that of a stand-alone two wire waveguide ~0.25 m^{-1}, while still small enough for the design of practical THz circuits. Finally, we note that using higher resolution SLA printers capable of reliable manufacturing of smaller ~ 500 μm diameter cylinders could further reduce the micro-encapsulated two-wire waveguide losses down to ~0.75-1.25 m^{-1} (by field) range theoretically.

For the convenience of fabrication, the encapsulated two-wire waveguide features two complementary parts, each one comprising one wire attached to a half cage using a deeply subwavelength dielectric support ridge (see Fig. 1. (c)). Although printing along Z-axis can greatly reduce the fabrication time, printing large diameter overhanging wire on a slender support ridge proved to be challenging. Therefore, each part was printed along the waveguide propagation direction (X axis) using 25 μm layer thickness of an ASIGA 2 Pro SLA printer. After polishing the ends of a fully cured structure, the inside of a cage was protected with a masking tape, while leaving only the plastic wire support surface exposed. Next, silver layer was deposited on top of the plastic using wet chemistry to form conductive surfaces. A two-wire waveguide was finally obtained by assembling the two metallized parts by sliding them into each other using V-grooves and V-ridges that were printed onto the cage to simplify alignment and connectorization (see Fig. 1. (c)). High quality 6 cm-long waveguide sections were then printed, while longer waveguides were assembled from such sections using another set of alignment and connectorization elements imprinted onto the cage end facets (see Figs. 2. (a) I and 2. (b)). Position and size mismatch between the two wires in the adjacent waveguide sections is mostly due to precision of the SLA printer and polishing imperfections, which is on the order of several tens of microns (example of a two-wire junction is shown in Fig. 2. (c)). While this can bring additional coupling losses, we expect that they will be small as the mode is mostly guided in the gap between the wires, which is almost hundred times larger in size than potential misalignment and size mismatch of the wires. Additionally, precise alignment of the encapsulated two-wire waveguide with the WR6.5 waveguide flange (of a conical horn antenna) can be realized by aligning precision screw holes in a flange with judiciously positioned holes in a 3D printed cage (Fig. 2. (a) II and 2(b)).

Additionally, grain size of the deposited silver layer is on the order of several tens of nanometers [51], while the metal layer is several microns thick. Thus, metal surface roughness would be mostly determined by the roughness of the printed wire-shaped support, which is on the order of several tens of microns. While surface roughness of the metal layer that supports SPP can bring additional scattering loss, such roughness is on a scale much smaller than the wavelength of THz light, thus we expect that waveguide losses will be mostly defined by the quality of the nanostructured metallic coating rather than by the imperfections in the shape of a printed wire support.

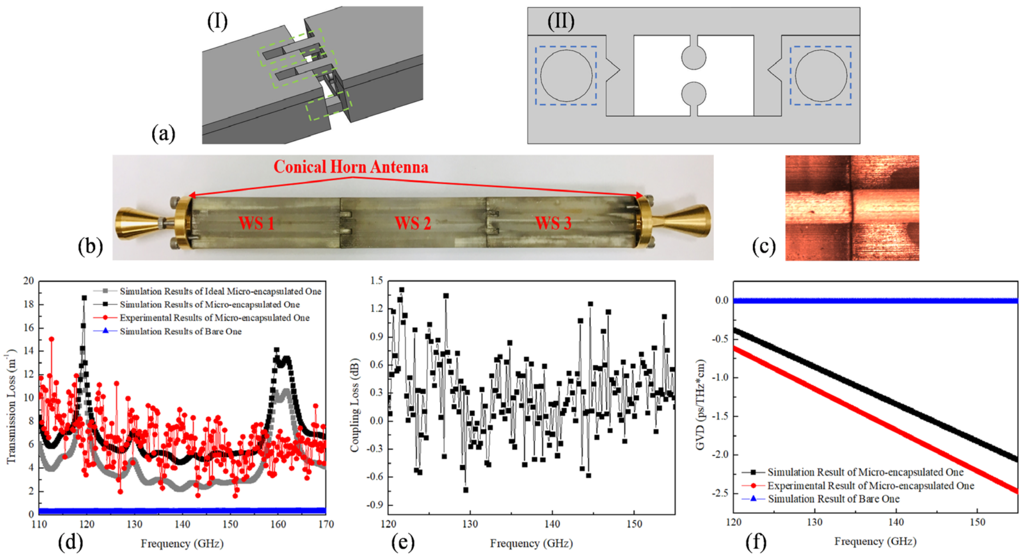

Fig. 2. (a) I: Schematic of an interconnect between two plasmonic waveguides. In green dotted region are shown the alignment elements. II: Schematic of the end face of an encapsulated two-wire waveguide. In the blue dotted regions shown are the

screw holes with depths of 5 mm for precision alignment and connectorisation with the WR6.5 waveguide flange (conical horn antenna). (b) An 18 cm-long straight two-wire waveguide assembled by connecting three 6 cm-long sections. The two ends of the composite waveguide are fitted with the WR6.5CH-conical horn antennas (Virginia Diodes, Inc.). (c) An enlarged view of the junction between the two wires in a butt-coupling arrangement between the two neighboring waveguide sections. (d) Comparison of the numerical modal losses (by field) for the THz SPP wave and the measured transmission loss of a straight two-wire waveguide using cut-back measurements. (e) Experimentally measured insertion loss (by power) for two butt-coupled waveguides. (f) Numerical simulation and experimental results for the modal GVD for a straight two-wire waveguide.

3. Optical characterization of the 3D printed two-wire waveguide components

3.1 Straight two-wire waveguides

The two-wire waveguide transmission losses (see Fig. 2. (d)) and coupling losses (see Fig. 2. (e)) were deduced from the cut-back measurement using composite three-section waveguides similar to the one shown in Fig. 2. (b) (see Supplementary Material B.1 for details). The measured transmission loss (by field) is almost constant ~6 m^{-1} in the 120-170 GHz frequency range (red curve in Fig. 2. (d)), which is almost twice as high as losses predicted by numerical simulations using Drude model of bulk silver (grey curve in Fig. 2. (d)). Significant difference between experimentally measured surface plasmon losses in THz and theoretically computed ones using bulk Drude-Lorentz model of metals is a well-known problem, which is attributed to the surface imperfections and limitations of a Drude model at the metal surfaces [52-55]. In the case of silver layers deposited using wet chemistry (as used in our work), their metal conductivity can be significantly smaller than that of a fine silver sheet because of the nano/micro-crystallization and oxidation effects. While it was demonstrated that for such nanostructured surfaces Drude-Smith model of metal permittivity could provide more accurate numerical results for THz surface waves, this model is experiment-specific and lacks universality [14,56]. To make comparison between experimental and numerical work more realistic, and considering that operational frequency range of our devices is relatively narrow (~110-170 GHz), we retain the simple Drude-Lorentz model of silver for our simulations, while simply fitting the damping factor to achieve the best fit of our numerical simulations with the experiment (black and red curves in Fig. 2. (d)). In particular we find that to reproduce experimental loss of a straight plasmonic waveguide, the damping factor should be increase by factor of 50, the value $\gamma = 2\pi \cdot 2.69e14$ Hz that we use in all our following simulations throughout the paper. We then compare losses of a stand-alone two-wire waveguide with that of an encapsulated waveguide of identical geometry (blue and red curves in Fig. 22. (d)). We find that stand-alone two-wire waveguides (where ohmic losses dominate) have somewhat smaller, while nevertheless comparable losses to those of encapsulated waveguides that feature additional loss contribution due to resin cage absorption.

One significant discrepancy between the numerical simulations and loss measurements of micro-encapsulated two-wire plasmonic waveguides is the presence of two strong absorption peaks as predicted theoretically at 119 GHz and 161 GHz with spectral widths of 1.7 GHz and 3.1 GHz (FWDM) respectively. These peaks are due to accidental degeneracy of the dispersion relations of the SPP mode and the high-loss bulk modes of a resin cage. In the vicinity of the degenerate frequency (phase matching point), the SPP mode hybridizes with the mode of a resin cage, and the resultant dispersion relations of the supermodes exhibit classic avoided crossing behavior. Bandwidth of a loss peak is proportional to the coupling strength between the SPP and a cage mode. The exact shapes of such peaks and their positions are highly sensitive to the scattering losses and structure inhomogeneities (surface roughness) and can easily disappear completely (especially for the narrow peaks) due to decoherence brought by such imperfections [40]. Therefore, we are not surprised by the absence of such peaks in the measured spectra due to narrow bandwidths of peaks, which is most probably caused by the effects of roughness of the printed structures, as well as cage surface contamination with silver residue during wet chemistry processing. In fact, a more careful implementation of a waveguide with polishing and better controlled wet chemistry deposition of metal layer allows for observation of avoided crossing resonances, thus making us confident about the good correspondence between the theoretical and experimental results, as well as about our overall understanding of a system (see Supplementary Material A for details).

In addition to waveguide losses, one can also extract inter-waveguide coupling losses due to mismatch in the relative size and positions of the neighboring waveguide sections by performing two separate cutback measurements that use waveguide sections of different lengths (see Supplementary Material B.1 for details). The coupling loss (by power) data is measured in the 120 - 155 GHz range (see Fig. 2. (e)), with a typical power loss value in the ~0.4 dB per connection, which is significantly smaller than a single waveguide section transmission loss (~3 dB by power for a 6 cm-long section). This allows connecting ~8 sections (total waveguide length of ~0.5m) before it can start significantly affecting the power budget, thus making us confident that connectorization of many two-wire waveguide-based components is feasible when designing complex THz processing photonic circuits.

Finally, in Fig. 2. (f) we present experimental data and numerical simulation of the GVD of the SPP mode of a two-wire encapsulated waveguide in the 120 – 155 GHz spectral range by using the following definition:

$$GVD = \frac{\partial^2 \beta(\omega)}{\partial \omega^2} = \frac{\partial^2 (n(\omega) \cdot \omega / c)}{\partial \omega^2} \qquad [3]$$

One of the reasons why we pursued development of the plasmonic THz circuits is because of the very small GVDs of the THz SPP waves guided by the classical stand-alone two-wire waveguides [36], which potentially allows processing of extreme data bitrates without scrambling the signal due to temporal pulse dispersion. In the case of encapsulated two-wire waveguides, the GVD of an SPP mode will be higher than that of a bare two-wire waveguide due to partial overlap of the SPP modal fields with the cage. As shown in Fig. 2. (f), measured GVD of an encapsulated two-wire waveguide is in the 1-2 ps/THz·cm, which is also in agreement with the results of numerical simulations. While this value is significantly higher than that of a stand-alone two-wire waveguide (less than 0.01 ps/THz·cm) which is shown (blue curve in Fig. 2. (f)), it is nevertheless much smaller than GVD of most alternative THz waveguides which is normally in the 10's ps/THz·cm range. For all these reasons, we believe that encapsulated two-wire waveguides offer a viable platform for building signal processing THz photonic circuits.

3.2 Two-wire waveguide bends

The curved waveguides are of critical importance for building practical photonic circuits and they are integral part of various components such as splitters, couplers, ring resonators, optical delay lines, etc. [42,57-59]. Moreover, curved waveguides serve as interconnects between various components of the high-density photonic circuit [60]. Unfortunately, modes guided by curved waveguides are often leaky, and they are prone to higher radiation losses for tighter bends [61]. Additionally, mode of a bent waveguide has somewhat different field distribution from that of a straight waveguide, thus coupling between straight and bent waveguides also leads to back reflections and radiative insertion loss, which again is more pronounced for tighter bends. All these negative effects associated with waveguide bends are typically mitigated by increasing the mode confinement which can be achieved, for example, by employing high refractive index contrast waveguides (ex. silicone photonics) [62,63]. Importantly, plasmonic modes of a two-wire waveguide show relatively strong confinement in the gap between the two metallic wires, and we find that effect of bending in such waveguides in less pronounced compared to many other THz waveguides such as single wires [64], tube-shaped hollow core waveguides [65] and subwavelength fibers [3]. In what follows we present numerical and experimental studies of bending loss in the encapsulated two-wire waveguides and demonstrate that it is significantly smaller than that in the case of stand-alone two-wire waveguides. We attribute this finding to a stronger confinement of the plasmonic mode in the case of encapsulated wires.

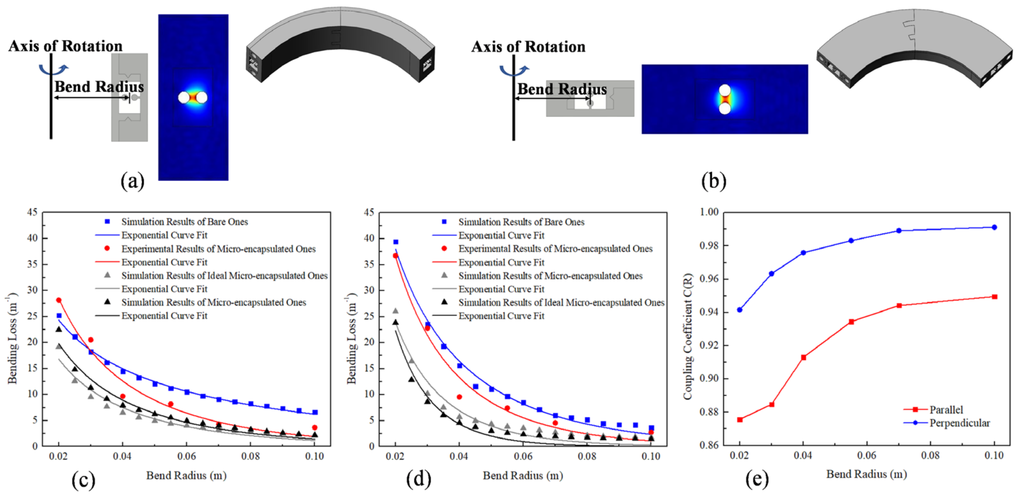

Fig. 3. (a) and (b) Schematics of the two types of the two-wire waveguide 90° bends of 4 cm bend radius and the corresponding modal field distributions |*E(x,y)*| of the THz SPP waves at 140 GHz. (c) and (d) Bending losses (by field) of the two types of the waveguide bends. (e) The coupling coefficient $|C(R)|^2$ (by power) between the encapsulated two-wire waveguide bends and the straight one.

In Figs. 3. (a) and (b) we show schematics of the two types of bends that differ from each other by the relative orientation of the bend rotation axis and the two wires. When plotting the modal electric field distributions |E|, we note that their maxima are somewhat shifted from the center of the gap between the two wires and away from the rotational axis, which is a well-known effect of the bend on modal fields, and is also the principal reason for the bend insertion losses. The transmission (by power) through a waveguide bend connectorized on both sides to straight sections of the same waveguide can be quite generally written as:

$$T = \left|C(R)\right|^2 \cdot \left|C(R)\right|^2 \cdot \exp\left(-2\alpha_{st} l_b\right) \exp\left(-2\alpha_b(R) \cdot l_b\right) \qquad [4]$$

Where R is the bend radius of the two-wire waveguide bend, l_b is the length of the waveguide bend, α_{st} is the transmission loss (by field) of a straight waveguide, $\alpha_b(R)$ is an additional loss (by field) due to bending. $C(R)$ is the coupling coefficient (by field) computed using (1) using the longitudinal flux operator average between the modal fields of the curved and straight waveguides, while $1-\left|C(R)\right|^2$ is the insertion loss (by power) on each side of the bend/straight waveguide connection.

The curved two-wire waveguides were studied using 2D axisymmetric models in COMSOL finite element modeling software that allows to compute complex effective refractive indices of the bend modes. The Ag layer was modeled using IBC with the fitted Drude-Lorentz model (2). Figs. 3 (c) and (d) show the results of numerical simulations of bending losses as a function of bending radius of stand-alone and encapsulated two-wire waveguides as well as their corresponding analytical fit using [66,67]:

$$\alpha_b(R) = \mathrm{A} \cdot \exp(-\mathrm{B} \cdot R) / \sqrt{R} \qquad [5]$$

Compared to the stand-alone two-wire waveguide bends, the encapsulated two-wire waveguide bends show considerably lower bending losses due to enhanced modal confinement brought by the resin cage (blue and black curves in Fig. 3. (c)), as explained in Section 2. Moreover, bending loss is not sensitive to the value of the damping constant (gray and black curves in Fig. 3. (c) computed using γ_b and γ_s respectively). Finally, Fig. 3. (e) shows the power coupling coefficient $|C(R)|^2$ that was computed using modal matching approach Eq. [1] [43], by expending the mode of a straight encapsulated waveguide into the modes of a bent one (assuming no back reflections).

As a result, we find that bends with the axis of rotation perpendicular to the line connecting the two wire centers (see Fig. 3. (a)) feature somewhat smaller bending losses and larger coupling coefficient with the straight waveguides than the other bend type (see Fig. 3. (b)). This is due to tighter confinement of the guided mode in the case of the first bend type. Indeed, the effect of the bend is to shift the modal field away from the rotational axis of the bend toward infinity. In case of a bend in Fig. 3. (a), in doing so the mode encounters a metal surface of a wire, while in the case of a bend in Fig. 3. (b) there is nothing to limit such a shift. Therefore, modes of such a bend show stronger confinement in the core (inter-wire gap), which also results in lower bending losses.

Next, we experimentally studied losses of the two bend types using 90° bend sections for the bend radii in the range of 2-10 cm at 140 GHz. Due to limitation of SLA 3D printing, 90° bends were realized by assembling two 45° sections of the same bend radius (see Figs. 3. (a) and (b)). The measurements are summarized in Figs. 3. (c) and 3. (d) (see details in Supplementary Material B.2). While experimental loss is somewhat higher than the theoretical one, the overall tendency is well reproduced. Discrepancies between the experimental and numerical results can be attributed to the effect of printing imperfections such as discrete shape definition by the SLA printer, as well as surface warping during postprocessing curing step.

3.3 Two-wire Waveguide Bragg Gratings (WBGs)

THz Waveguide Bragg Gratings are of great value for building signal processing components for THz communications [43]. WBGs are often used as band-reject filters, while WBGs with defects are used as band-pass filters. Thus, integration of even the simplest WBGs into THz photonic circuits can enable such advanced signal processing functionalities as noise filtering or channel adding or dropping when using Frequency Division Multiplexing (FDM). In what follows, we demonstrate design and fabrication of strong two-wire waveguide Bragg gratings with a stop-band of up to 20 GHz for applications in THz communications within the FDM paradigm. With the operation frequency in the lower THz band of 0.1 – 0.3 THz, one can pack ~10 of 20 GHz-wide channels each supporting up to 20 GBs data rates. The lower THz band is easily accessible both with electronics [3,68-70] and optics-based THz communication systems [71] with data modulation rates per channel as high as 40 GBs. We therefore believe that FDM approach in the lower THz band can be a viable approach for multi-channel data transmission with total data rates exceeding several 100s GBs.

To fabricate strong WBGs based on the two-wire waveguides, we place a low-loss dielectric substrate featuring a periodic pattern of metallic stripes into the gap between the two wires. This arrangement results in strong overlap of the waveguide modal fields with the grating region, and as a consequence, wide stop-bands of up to 10% (of the center frequency) can be achieved. While a variety of methods exist for the fabrication of metal patterns on dielectric substrates including laser engraving, lithography and etching [72-74], such techniques require relatively expensive infrastructure. In this work, we explored an alternative low-cost and simple hot stamping technique for WBG fabrication. The main advantage of this technique is its similarity to 3D printing as it allows rapid prototyping and extensive fine tuning of the grating geometry with only a minimal time and material expenditures. Particularly, as a substrate for the metal grating we used 100 μm-thick printing paper (Premium Laser Print, Hammermill Inc, n_p=1.45, α_p[cm^{-1}]=41.33·(ω[THz])^2+2.039 (by field) [37]). The periodic metal pattern was deposited by first printing the required pattern in ink on both sides of the paper symmetrically (laser printer Xerox Phaser 6180MFP), and then transferring the metal/polymer composite from the thermofoil sheet (Deco foil, Thermoweb Inc) onto the ink-covered paper region. The transfer was achieved by placing the paper in direct contact with thermofoils and heating inside the thermal laminator (Fusion 1100L, Swingline Inc). The end result is a periodic pattern of a few μm-thick aluminum/thermoplastic composite transferred on top of the printed ink pattern [75]. To accommodate thus fabricated grating, the enclosure of a 3D printed two-wire waveguide shown in Fig. 1. (c) was slightly modified to include two narrow slits in the resin cage throughout the whole length of a waveguide. The grating was then inserted into the slits and self-aligned to be in the center of the air gap between the wires (see Fig. 4. (a)).

Operation of thus fabricated gratings is easy to understand using coupled mode theory by considering three principal modes propagating in the two sections of the WBG. Particularly, Fig. 4. (b) I shows schematic of the two sections comprising a single period of the WBG. The first section of width w_1 features a two-wire waveguide with a blank paper sheet in between. The first section transverse crossection is shown in Fig. 4 (b). II. As the optical thickness of a blank paper (~145 μm) is much smaller than the gap size (~660 μm) and the wavelength of light used in our experiments (at 140 GHz λ~2 mm), the paper substrate itself does not modify significantly the modal field distribution in the gap between the two wires. Therefore, the effective RI of the fundamental mode propagating in section 1 (propagation constant of β_1) is still close to 1 and the modal field distribution resembles that of an empty two-wire waveguide (compare Figs. 4. (b) IV and 1 (d)). At the same time, due to the paper orientation, the modal electric field is mostly perpendicular to the paper surface, thus amplitude of the electric field in the paper is reduced compared to that in the air $|E_p| \approx |E_a|/n_p^2 \sim |E_a|/2$. Transmission spectrum through a two-wire waveguide with the inserted paper is therefore close to the one without the inserted paper, as seen in Fig. 4. (e) (orange curve).

The second section of width w_2 additionally features thin metal plates on both sides of a paper sheet. The second section transverse crossection is shown in Fig. 4 (b). III. In Section 2 of the grating, two kinds of modes are supported. As the paper dielectric substrate is sandwiched by two metal plates, one of the modes (see Fig. 4. (b) V) with propagation constant β_2 propagates directly between the metal plates, thus resembling a TEM-like mode of a Parallel Plate Metallic Waveguide. As the corresponding modal field is mainly localized in the paper, mode 2 effective RI is close to that of the paper 1.45. The other mode propagating in section 2 (mode 3 with β_3) is mostly confined to the air region between the metal wires and metal plates. Its modal field distribution and effective RI are similar to those of the mode 1 of section 1 (compare Figs. 4. (b) IV and VI). At the interface between two sections of a single period, the power coupling coefficient δ between highly dissimilar modes 1 and 2 can be computed using mode matching method Eq. [1], [43]. For geometries considered in this paper we find δ~0.03–0.06 depending on the configuration. At the same time, power coupling coefficient between two similar modes 1 and 2 is high, and assuming small reflection and negligible scattering (radiation) loss at the interface between two sections it is $\sim 1-\delta$. It can be then show using rigorous coupled mode theory that the forward propagating modal fields at the beginning of any period $|F(x)\rangle$ will be related to the corresponding fields at the beginning of the next period $|F(x+P)\rangle$ as:

$$\begin{aligned} &|F(x+P)\rangle \approx |F(x)\rangle \cdot \exp(i\beta_1 w_1) \cdot [\delta \cdot \exp(i\beta_2 w_2) + (1-\delta) \cdot \exp(i\beta_3 w_2)] \approx \\ &\approx |F(x)\rangle \cdot \exp(i\beta_1 w_1 + i\beta_3 w_2) \cdot \left[1 - \delta \cdot \left(1 - \exp\left(i(\beta_2 - \beta_3) w_2\right)\right)\right] \end{aligned} \quad [6]$$

Physically this means that mode 1 of section one excites two modes 2 and 3 in section two, which then propagate with different phase velocities. If the two modes recombine destructively at the end of the period, this will resulting in the strong back-reflection, and the grating will be at the stop band. Therefore, to minimize transmitted power through grating one has to choose the width w_2 of section 2 so that:

$$(\beta_3 - \beta_2) w_2 = \pi \cdot (2m_w + 1) \quad , \quad m_w \in \mathbb{N} \quad [*]$$

Additionally, remembering that the modes 1 and 3 are similar (Figs. 4. (b) IV and VI) and have very similar proipagation constants $\beta_1 \approx \beta_3$, and that the grating period is $P = w_1 + w_2$, then, for the forward propagating field we can write:

$$|F(x+P)\rangle \approx |F(x)\rangle \cdot \exp(i\beta_1 P) \cdot [1 - 2\delta] = |F(x)\rangle \cdot \exp(i\beta_g P)$$

$$\beta_g = \beta_1 + i\frac{2\delta}{P}$$

which shows exponential decay of the fields along the grating, and it also satisfies the Block form assuming complex propagation constant of the WBG. Finally, as propagation along the grating is mostly dominated by the modes 1 and 3 with propagation constant β_1, then the reciprocal wavevector of the grating has to match the difference between WBG forward and backward propagating modes, thus resulting in additional condition for the grating design:

$$2\beta_1 = \frac{2\pi}{P} m_p \quad , \quad m_p \in \mathbb{N} \quad [**]$$

Example of the numerical study of gratings designed using resonant design conditions Eqs. [*,**] is presented in Supplementary Material D. Results of transmission and reflections simulations using COMSOL finite element formulation with ports confirm the validity of our understanding of the grating operation principles. Note that the resonant conditions [*,**] result in the most pronounced stop bands and strong reflections, while there are other resonant conditions possible when phase matching the forward propagating mode of a two wire waveguide with that of a forward or backward propagating modes of a metal plate waveguide. The design complexity and numerous possible resonances in a three-mode grating merit a separate paper, while what follows just aims at presenting some example of WBGs based on the combination of two-wire and parallel plate waveguides.

Next, we detail the two-wire waveguide Bragg gratings featuring broad and pronounced transmission dips at 140 GHz. Such WBGs can serve as efficient band-rejection filters in the THz communication circuits. The WBGs are first studied using 3D modeling frequency domain tool with ports within COMSOL Multiphysics. Because of two reflection symmetry planes, only a quarter of a structure together with Perfect Electrical Conductor (PEC) and Perfect Magnetic Conductor (PMC) boundary conditions can be used. The metalized patterns on paper are defined using the IBC boundary condition with Drude-Lorentz model for bulk Aluminium. In our simulations, the THz light is launched using port boundary condition at the input facet of the WBGs containing 7 periods. By monitoring the power transmission coefficient at the other facet of the WBGs ($|S21|^2$), we find, for example, that gratings with a period of 1.5 mm and a metalized-paper section width w_2 of 0.7 mm feature pronounced transmission dips at 140 GHz (see Figs. 4. (d) and 4. (e)). At the same time, power reflection coefficient ($|S11|^2$) in such design is small (less than 10%). A more detailed analysis show that in such a grating the forward propagating mode of a metal plate waveguide is matched to the backward propagating mode of a metal plate waveguide, that has only a small coupling with a backward propagating mode of a two-wire waveguides. Thus, such a grating, while featuring a large stop-band, is also characterized by low reflection into a two-wire waveguide that feeds it.

In our experiments we used gratings of different lengths that featured a periodic sequence of metal strips on a paper substrate that was placed into a gap of a 10-cm two-wire waveguide. It was then characterized in a setup detailed in Supplementary Material B. 1. The grating transmittance was obtained by comparing the transmission spectra of the two-wire waveguide with and without the gratings (see Fig. 4. (e)). A pronounced transmission dip at 140 GHz featuring a spectral width of 32 GHz (FWDM) and a minimum relative transmittance below 10^{-2} is obtained using the grating with a length of 5 cm. Additionally, when increasing the grating length to 10 cm, such transmission dip becomes even more pronounced, however, standing waves caused by the multiple reflections inside the silicon lens integrated into photomixers of our CW-THz spectroscopy setup interferes with the observation of the broadband transmission dip [40] and results in ~4 GHz equi-spaced intensity ripples.

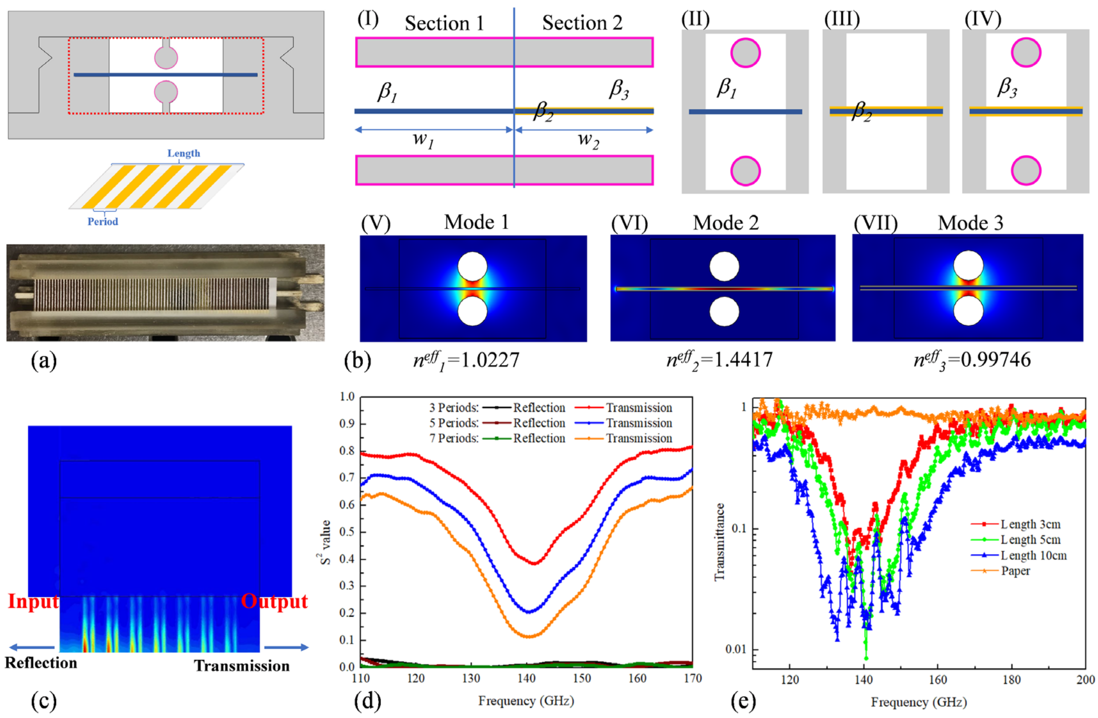

Fig. 4. (a) Schematic of the two-wire waveguide Bragg grating (top) and a photo from the top with half of the cage removed (bottom). (b) (I) Schematic of a single period of the WBG that comprises two sections, one containing a bare paper sheet, and the other one containing metallized paper with the corresponding transverse cross-sections shown in (II) and (III). The electric field distributions (|E|) of principal modes propagating in section one - Mode 1 (IV), and section two - Mode 2 (V), and Mode 3 (VI) at 140 GHz. (c) The simulated modal electric field distribution (|E|) of a WBG in the symmetry plane in the mid gap between the two wires at 140 GHz. (d) The simulated power transmission $|S21|^2$ and reflection $|S11|^2$ coefficients for WBGs with different number of periods. (e) The experimental transmittance of the corresponding WBGs of different lengths inserted into a 10 cm-long two-wire waveguide.

4. The THz plasmonic circuits

In this section, we demonstrate the possibility of building highly reconfigurable plasmonic circuits using as an example THz splitter/multiplexer and a two-channel ADM.

4.1 THz Splitter/Multiplexer

A Y-shaped THz splitter/multiplexer was fabricated by fusing two 90° two-wire waveguide bends of 4 cm bending radius (axis of rotation parallel to the line connecting the wire centers) as shown in Fig. 5. (a). Furthermore, the two curved sections are terminated with short 0.5-cm sections of a straight waveguide for the ease of connectorization with other components. Such a coupler can be used either as a broadband 50/50 splitter or a multiplexer of two data streams.

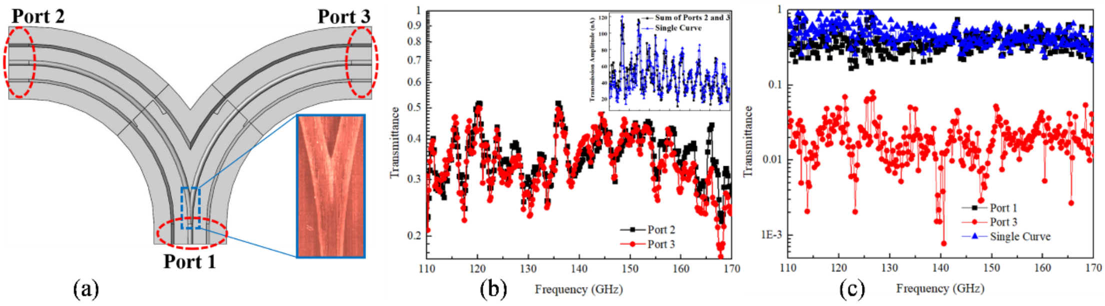

Fig. 5 (a) Schematic (half) of a Y-shaped splitter/multiplexer that uses two fused two-wire waveguide bends. In red dotted regions are the 0.5-cm section of straight waveguides. Inset: photo of the two fused wires in a blue dotted region of a schematic. (b) Transmittance of the output ports 2 and 3 with the incident THz light in port 1. Insert: comparison of the two transmissions, one (black) is obtained by summing the outputs of the ports 2 and 3 when light is launched into port 1, while the other one (blue) is obtained by measuring a single bend section with the equivalent geometry of a half splitter (shown in Fig. 3. (b)), thus signifying a minimal scattering loss at a Y-junction. (c) Transmittance of the output ports 1 (black) and 3 (red) when the THz light is launched into port 2, comparison with transmittance of a single bend section of equivalent geometry (blue) shown in Fig. 3. (b).

In the first experiment, we test Y-coupler operation in the splitter mode. The THz light is launched into port 1 via a WR6.5 conical horn antenna, then divided in the Y-shaped splitter, and finally registered at ports 2 and 3 (each featuring a WR6.5 conical horn antenna). Fig. 5. (b) shows the transmittances of the output ports, which are obtained by dividing the transmission spectra (by field) of light coming out from ports 2 and 3 by that of the THz light launched into port 1 (for more details, see Supplementary Material E). The data shows that transmittances of the two output ports are very similar with only few percentage difference in the 100-200 GHz operation frequency range.

In the second experiment, we test Y-coupler operation in the multiplexer mode. The THz light is launched into port 2 (or port 3), then travels through the Y-junction, and finally leaves the component through port 1 and partially through unused port 3 (or port 2, correspondently). For example, Fig. 5. (c) shows transmittances of the ports 1 and 3, which are obtained by dividing the transmission spectra (by field) measured at these ports by the spectrum of the THz light launched into port 2. Note that parasitic transmission through port 3 (due to back-scattering at the Y-junction) is much weaker (on average by -50 dB by power) than intended forward signal transmission through port 1, which signifies that the developed component can be used as a 2 x 1 multiplexer. Furthermore, by comparing the net (sum) intensity of THz light measured at the output ports 1 (and 2) of the Y-coupler to the light intensity transmitted through a single bend of identical geometry (see blue curves in Figs. 5. (b) insert and 5. (c)), we conclude that the average insertion loss brought by the Y-junction is small ~0.3 dB at ~140 GHz.

4.2 THz Add-Drop Multiplexer

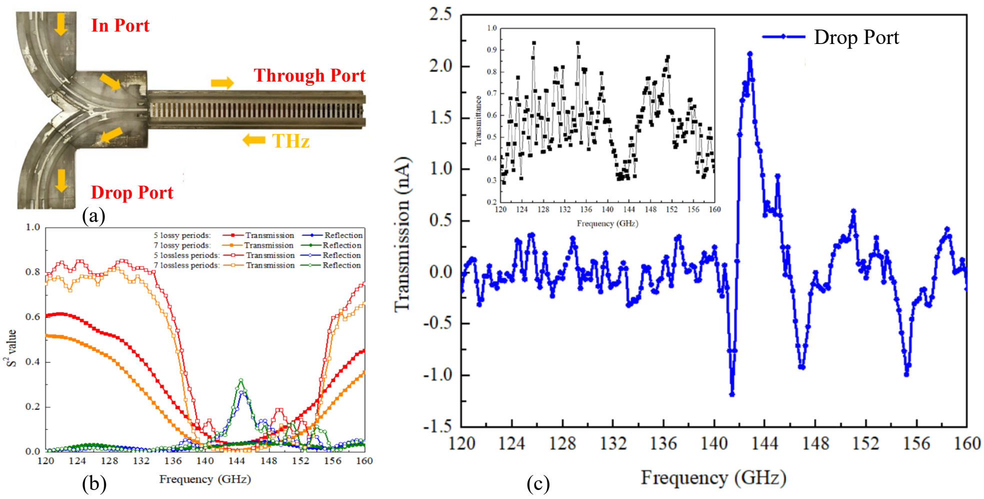

Fig.6. (a) The two-wire waveguide-based ADM composed of an Y-coupler and a WBG. (b) The numerical results of the transmission ($|S21|^2$) and reflection ($|S11|^2$)

of WBGs with a period of 2.3 mm and a duty cycle of 55%. (c) Recorded spectrum (field amplitude) of the ADM measured at the Drop port. Inset: the transmittance (by field) of the stand-alone WBG that is integrated into the ADM.

The Add-Drop Multiplexer is a key building block in any communication systems that uses Frequency Division Multiplexing (FDM). Many ADM designs in the near-infrared telecommunication band use fiber Bragg gratings and circulators [76], a concept that we translate in our current work into THz range. Alternatively, THz ADMs were also build using photonic band gap materials and ring resonators [23,77]. Such devices, however, were obtained using complex and costly microfabrication processes in which high-resistivity float zone silicon wafer was machined and then recovered with gold layer through eutectic bonding. Although a much simpler 3D printing technique can be used to make similar structures, unfortunately, plastics compatible with high-resolution stereolithography are strong absorbers of the THz light. While some low-loss thermoplastics such as Polypropylene [3] are compatible with FDM additive manufacturing, resolution of such devices is generally not adequate for fabrication of ADM in the THz frequency range.

In this section, as a proof of concept, we demonstrate a simple ADM of ~2.8 GHz bandwidth (FWHM) that operates at ~140 GHz by integrating a Y-coupler and a WBG based on two-wire waveguide technology detailed earlier. The ADM is shown in Fig. 6. (a). A signal featuring several mixed stand-alone channels at different frequencies (FDM modality) is launched into the In port. After propagation through a curved waveguide of a Y-coupler, the signal arrives to a WBG where the channel in the grating stopband is back reflected, while the rest of the channels continue into the Through port. In the absence of a THz circulator, the reflected channel is then split 50/50 by the Y-coupler and it finally arrives to the Drop port. Note that THz circulators have been demonstrated earlier (ex. [78]) and they are fully compatible with the two-wire waveguide base technology used in this work.

At first, we study the WBGs used in our ADM prototype with COMSOL Multiphysics. By analyzing the transmission and reflection spectra of gratings featuring different pitches, we find that transmission dips and significant reflection peaks can be obtained at ~140 GHz using gratings with a period of 2.3 mm and a duty cycle of 55% (w_2=1.27 mm) (see Fig. 6. (b)). Here we present simulation using lossy versus loss-less paper substrate material. Compared with the grating of 1.5 mm period discussed earlier (see Fig. 4. (d)), gratings used in our ADM prototype feature somewhat narrower stop bands, while at the same time they feature significant reflected power in the stop band ($|S11|^2$~30% loss-less paper, and $|S11|^2$~6% lossy paper), which makes them suitable for building ADMs. We note that paper loss has significant negative effect on the reflected power, and in the future work we will look for alternative substrates for our gratings. Experimentally, a 6.9 mm-wide paper sheet featuring 43 grating periods of 2.3 mm pitch and symmetric arrangement of metal stripes on both sides of the paper substrate was prepared as described in Section 3.3. A resultant 10 cm-long WBG was measured and showed a minimal relative transmittance of 0.3 with ~4 GHz (FWHM) transmission dip at the Bragg frequency of 142.6 GHz (see Fig. 6(c) Inset). Finally, Fig. 6. (c) shows the measured spectra at the Drop port of the ADM that uses the abovementioned WBG in the Through arm of the device (for details of the measurement see Supplementary Material E). The dropped target range ~141-145 GHz is clearly visible at the Drop port of the ADM despite low reflection efficiency of the grating.

Finally, our simulations suggest that considerably more efficient (in reflection) gratings can be designed using classic quarter wave condition for each section in the period, or even using more relaxed design criteria [*,**], however, such gratings cannot be reliably manufactured using a simple hot stamping technique that we have explored in this paper as they require significantly smaller metallic features and lower-loss substrates. We therefore consider the results of this section as a proof of principle with a clear path for optimization to be pursued in our future works.

5. Conclusion

In this work, 3D printed micro-encapsulated two-wire THz plasmonic waveguide components and circuits have been investigated theoretically and experimentally. Modular THz components and reconfigurable circuits are built based on two-wire waveguides featuring two metallized plastic wire substrates suspended in air on deeply subwavelength supports and encapsulated inside a protective resin cage. Such components are fabricated using highly precise, efficient and low-cost SLA 3D printing enhanced with wet chemistry metal deposition technique. Using CW-THz spectroscopy, we first characterised the transmission loss and the GVD of straight waveguides at 140 GHz which were ~6 m^{-1} (by field) and -1.5 ps/THz·cm respectively. Next, the bending loss of bent two-wire waveguides was characterized experimentally as a function of bending radii for two different types of bend geometry. It was concluded that the presence of encapsulating cage significantly reduced bending loss due to stronger confinement of light in the gap between the two wires compared to the case of stand-alone two-wire waveguides. We then find that even for small bending radius ~5cm, experimental bending loss does not exceed ~10 cm^{-1} (by field). Next, we detailed two-wire waveguide Bragg gratings that feature a thin paper sheet with periodic sequence of metal strips placed in the gap between two wires. Metallized gratings were fabricated using a rapid prototyping hot stamping technique using thermofoils, laser printed templates and a laminator. Experimentally, we showed that event short 5 cm-long WBGs of this design can exhibits transmission dips with minimal relative transmittance below 10^{-2} and a spectral width of 32 GHz. Finally, two kinds of THz plasmonic circuit prototypes were demonstrated, including a Y-shaped THz splitter/multiplexer that employed two coalescing waveguide bends, as well as an ADM that employs a reflective WBD. Experimentally, we find that the Y-shaped coupler features a negligible insertion loss (<0.5 dB) and transmission loss almost identical to that of a stand-alone bend section employed in its design. Finally, we find experimentally that an ADM has exhibits a designed drop functionality with a spectral bandwidth of 2.8 GHz at the Bragg frequency of ~140 GHz. Based on our findings we, therefore, conclude that proposed 3D printed THz two-wire waveguides and components based on such waveguides present a viable technology for the robust, cost effective and highly reconfigurable THz optical circuits for signal processing, and sensing applications.

Reference

[1] Kleine-Ostmann, T. and Nagatsuma, T., 2011. A review on terahertz communications research. *Journal of Infrared, Millimeter, and Terahertz Waves*, *32*(2), pp.143-171.

[2] Ghasempour, Y., Shrestha, R., Charous, A., Knightly, E. and Mittleman, D.M., 2020. Single-shot link discovery for terahertz wireless networks. *Nature Communications*, *11*(1), pp.1-6.

[3] K. Nallappan et al. Dispersion limited terahertz transmission links using rod-in-air subwavelength dielectric fiber.

[4] Chen, Z., Ma, X., Zhang, B., Zhang, Y., Niu, Z., Kuang, N., Chen, W., Li, L. and Li, S., 2019. A survey on terahertz communications. *China Communications*, *16*(2), pp.1-35.

[5] Taravati, S. and Caloz, C., 2016. Mixer-duplexer-antenna leaky-wave system based on periodic space-time modulation. *IEEE Transactions on Antennas and Propagation*, *65*(2), pp.442-452.

[6] Al-Bassam, A., Otto, S., Heberling, D. and Caloz, C., 2017. Broadside dual-channel orthogonal-polarization radiation using a double-asymmetric periodic leaky-wave antenna. *IEEE Transactions on Antennas and Propagation*, *65*(6), pp.2855-2864.

[7] Liu, L., Caloz, C. and Itoh, T., 2002. Dominant mode leaky-wave antenna with backfire-to-endfire scanning capability. *Electronics Letters*, *38*(23), pp.1414-1416.

[8] Caloz, C., Itoh, T. and Rennings, A., 2008. CRLH metamaterial leaky-wave and resonant antennas. *IEEE Antennas and Propagation Magazine*, *50*(5), pp.25-39.

[9] R. Mendis and D. M. Mittleman, "Comparison of the lowest-order transverse-electric (TE 1) and transverse-magnetic (TEM) modes of the parallel-plate waveguide for terahertz pulse applications," *Optics express,* vol. 17, no. 17, pp. 14839-14850, 2009

[10] Bowden, B., Harrington, J.A. and Mitrofanov, O., 2008. Low-loss modes in hollow metallic terahertz waveguides with dielectric coatings. *Applied physics letters*, *93*(18), p.181104.

[11] Harrington, J.A., George, R., Pedersen, P. and Mueller, E., 2004. Hollow polycarbonate waveguides with inner Cu coatings for delivery of terahertz radiation. *Optics Express*, *12*(21), pp.5263-5268.

[12] Jeon, T.I., Zhang, J. and Grischkowsky, D., 2005. THz Sommerfeld wave propagation on a single metal wire. *Applied Physics Letters*, *86*(16), p.161904.

[13] Williams, C.R., Andrews, S.R., Maier, S.A., Fernández-Domínguez, A.I., Martín-Moreno, L. and García-Vidal, F.J., 2008. Highly confined guiding of terahertz surface plasmon polaritons on structured metal surfaces. *Nature Photonics*, *2*(3), pp.175-179.

[14] Poulin, M., Giannacopoulos, S. and Skorobogatiy, M., 2019. Surface Wave Enhanced Sensing in the Terahertz Spectral Range: Modalities, Materials, and Perspectives. *Sensors*, *19*(24), p.5505.

[15] Mitrofanov, O., Tan, T., Mark, P. R., Bowden, B. & Harrington, J. A. Waveguide mode imaging and dispersion analysis with terahertz near-field microscopy. *Appl. Phys. Lett.* 94, 171104 (2009).

[16] Withayachumnankul, W., Fujita, M. and Nagatsuma, T., 2018. Integrated silicon photonic crystals toward terahertz communications. *Advanced Optical Materials*, *6*(16), p.1800401.

[17] Tsuruda, K., Fujita, M. and Nagatsuma, T., 2015. Extremely low-loss terahertz waveguide based on silicon photonic-crystal slab. *Optics express*, *23*(25), pp.31977-31990.

[18] Li, J., He, J. and Hong, Z., 2007. Terahertz wave switch based on silicon photonic crystals. *Applied optics*, *46*(22), pp.5034-5037.

[19] Yata, M., Fujita, M. and Nagatsuma, T., 2016. Photonic-crystal diplexers for terahertz-wave applications. *Optics express*, *24*(7), pp.7835-7849.

[20] Li, S., Liu, H., Sun, Q. and Huang, N., 2015. A tunable terahertz photonic crystal narrow-band filter. *IEEE Photonics Technology Letters*, *27*(7), pp.752-754.

[21] Hübers, Heinz-Wilhelm. "Terahertz technology: Towards THz integrated photonics." *Nature photonics* 4.8 (2010): 503.

[22] Yu, Xiongbin, et al. "Integrated circuits using photonic-crystal slab waveguides and resonant tunneling diodes for terahertz communication." *2018 Progress in Electromagnetics Research Symposium (PIERS-Toyama)*. IEEE, 2018.

[23] Fan, F., Hou, Y., Jiang, Z.W., Wang, X.H. and Chang, S.J., 2012. Terahertz modulator based on insulator–metal transition in photonic crystal waveguide. *Applied optics*, *51*(20), pp.4589-4596.

[24] Simakov, E. I., Earley, L. M., Heath, C. E., Shchegolkov, D. Y., & Schultz, B. D. (2010). First experimental demonstration of a photonic band gap channel-drop filter at 240 GHz. *Review of Scientific Instruments*, *81*(10), 104701.

[25] M. Roze, B. Ung, A. Mazhorova, M. Walther, and M. Skorobogatiy, "Suspended core subwavelength fibers: towards practical designs for low-loss terahertz guidance," *Optics express,* vol. 19, no. 10, pp. 9127-9138, 2011.

[26] S. Atakaramians *et al.*, "THz porous fibers: design, fabrication and experimental characterization," vol. 17, no. 16, pp. 14053-14062, 2009

[27] K. Nallappan, H. Guerboukha, Y. Cao, C. Nerguizian, and M. Skorobogatiy, "Experimental Demonstration of 5 Gbps Data Transmission Using Long Subwavelength Fiber at 140 GHz," in *2019 IEEE Radio and Wireless Symposium (RWS)*, 2019, pp. 1-4: IEEE.

[28] H. Bao, K. Nielsen, O. Bang, and P. U. J. S. r. Jepsen, "Dielectric tube waveguides with absorptive cladding for broadband, low-dispersion and low loss THz guiding," vol. 5, p. 7620, 2015

[29] N. Van Thienen, W. Volkaerts, and P. Reynaert, "A multi-gigabit CPFSK polymer microwave fiber communication link in 40 nm CMOS," *IEEE Journal of Solid-State Circuits,* vol. 51, no. 8, pp. 1952-1958, 2016.

[30] A. Dupuis, K. Stoeffler, B. Ung, C. Dubois, and M. J. J. B. Skorobogatiy, "Transmission measurements of hollow-core THz Bragg fibers," vol. 28, no. 4, pp. 896-907, 2011.

[31] R. Mendis and D. Grischkowsky, "Undistorted guided-wave propagation of subpicosecond terahertz pulses," *Optics letters,* vol. 26, no. 11, pp. 846-848, 20

[32] R. Mendis and D. M. Mittleman, "Comparison of the lowest-order transverse-electric (TE 1) and transverse-magnetic (TEM) modes of the parallel-plate waveguide for terahertz pulse applications," *Optics express,* vol. 17, no. 17, pp. 14839-14850, 2009

[33] M. Mbonye, R. Mendis, and D. Mittleman, "A terahertz two-wire waveguide with low bending loss," Appl. Phys. Lett. 95, 233506 (2009).

[34] Markov, A., Guerboukha, H. and Skorobogatiy, M., 2014. Hybrid metal wire–dielectric terahertz waveguides: challenges and opportunities. *JOSA B*, *31*(11), pp.2587-2600.

[35] Anthony, Jessienta, Rainer Leonhardt, and Alexander Argyros. "Hybrid hollow core fibers with embedded wires as THz waveguides." *Optics Express* 21.3 (2013): 2903-2912.

[36] A. Markov and M. Skorobogatiy, "Two-wire terahertz fibers with porous dielectric support," Opt. Express 21, 12729–12743 (2013).

[37] Yan, G., Markov, A., Chinifooroshan, Y., Tripathi, S.M., Bock, W.J. and Skorobogatiy, M., 2013. Low-loss terahertz waveguide Bragg grating using a two-wire waveguide and a paper grating. *Optics letters*, *38*(16), pp.3089-3092.

[38] Yan, G., Markov, A., Chinifooroshan, Y., Tripathi, S.M., Bock, W.J. and Skorobogatiy, M., 2013. Resonant THz sensor for paper quality monitoring using THz fiber Bragg gratings. *Optics letters*, *38*(13), pp.2200-2202.

[39] J. Li, K. Nallappan, H. Guerboukha, and M. Skorobogatiy, "3D printed hollow core terahertz Bragg waveguides with defect layers for surface sensing applications," Opt. Express 25(4), 4126–4144 (2017).

[40] Cao, Y., Nallappan, K., Guerboukha, H., Gervais, T. and Skorobogatiy, M., 2019. Additive manufacturing of resonant fluidic sensors based on photonic bandgap waveguides for terahertz applications. *Optics express*, *27*(20), pp.27663-27681.

[41] D. Jahn, M. Weidenbach, J. Lehr, L. Becker, F. Beltrán-Mejía, S. F. Busch, J. C. Balzer, and M. Koch, "3D printed terahertz focusing grating couplers," J. Infrared Millim. Terahertz Waves 38(6), 708–716 (2017).

[42] M. Weidenbach, D. Jahn, A. Rehn, S. F. Busch, F. Beltrán-Mejía, J. C. Balzer, and M. Koch, "3D printed dielectric rectangular waveguides, splitters and couplers for 120 GHz," Opt. Express 24(25), 28968–28976 (2016).

[43] Skorobogatiy, M., 2012. *Nanostructured and Subwavelength Waveguides: fundamentals and applications*. John Wiley & Sons.

[44] S. Pandey, B. Gupta, and A. Nahata, "Terahertz plasmonic waveguides created via 3D printing," Opt. Express 21(21), 24422–24430 (2013).

[45] Ma, Tian, et al. "Analog signal processing in the terahertz communication links using waveguide Bragg gratings: example of dispersion compensation." *Optics express* 25.10 (2017): 11009-11026.

[46] Kovacevich, D.A., Lei, L., Han, D., Kuznetsova, C., Kooi, S.E., Lee, H. and Singer, J.P., 2020. Self-Limiting Electrospray Deposition for the Surface Modification of Additively-Manufactured Parts. *ACS Applied Materials & Interfaces*.

[47] Pahlevaninezhad, Hamid, Thomas E. Darcie, and Barmak Heshmat. "Two-wire waveguide for terahertz." *Optics Express* 18.7 (2010): 7415-7420.

[48] Plasmonic hotocatalysis. *Reports on Progress in Physics*, *76*(4), 046401.Pahlevaninezhad, Hamid, and Thomas E. Darcie. "Coupling of terahertz waves to a two-wire waveguide." *Optics express* 18.22 (2010): 22614-22624.

[49] Zhang, X., Chen, Y. L., Liu, R. S., & Tsai, D. P. (2013).

[50] Wang, Kanglin, and Daniel M. Mittleman. "Metal wires for terahertz wave guiding." *Nature* 432.7015 (2004): 376-379.

[51] Wen, Tianfa, et al. "Investigation on roughness of silver thin films inside silica capillaries for hollow waveguides." *Materials Letters* 50.2-3 (2001): 124-128.

[52] Jo, J.S., Jeon, T.I. and Grischkowsky, D.R., 2013. Prototype 250 GHz bandwidth chip to chip electrical interconnect, characterized with ultrafast optoelectronics. *IEEE Transactions on Terahertz Science and Technology*, *3*(4), pp.453-460.

[53] Laman, N. and Grischkowsky, D., 2007. Reduced conductivity in the terahertz skin-depth layer of metals. *Applied physics letters*, *90*(12), p.122115.

[54] Nazarov, M. and Coutaz, J.L., 2011. Terahertz surface waves propagating on metals with sub-wavelength structure and grating reliefs. *Journal of Infrared, Millimeter, and Terahertz Waves*, *32*(10), p.1054.

[55] A. J. Shutler and D. Grischkowsky, "Gap independent coupling into parallel plate THz waveguides using cylindrical horn antennas," *J. Appl. Phys.*, vol. 112, no. 7, p. 073102, 2012.

[56] Cocker, T.L., Baillie, D., Buruma, M., Titova, L.V., Sydora, R.D., Marsiglio, F. and Hegmann, F.A., 2017. Microscopic origin of the Drude-Smith model. *Physical Review B*, *96*(20), p.205439.

[57] J. Ma et al., "Communications with THz waves: switching data between two waveguides," Journal

of infrared and millimeter waves, 2017.
[58] K. S. Reichel et al. "*A broadband terahertz waveguide T-junction variable power splitter*", Scientific reports, 2016.
[59] Wang, Bing, and Guo Ping Wang. "Plasmonic waveguide ring resonator at terahertz frequencies." *Applied physics letters* 89.13 (2006): 133106.
[60] Yu, Bo, et al. "High-efficiency micromachined sub-THz channels for low-cost interconnect for planar integrated circuits." *IEEE Transactions on Microwave Theory and Techniques* 64.1 (2015): 96-105.
[61] Saijonmaa, J., and D. Yevick. "Beam-propagation analysis of loss in bent optical waveguides and fibers." *JOSA* 73.12 (1983): 1785-1791.
[62] Vlasov, Yurii A., and Sharee J. McNab. "Losses in single-mode silicon-on-insulator strip waveguides and bends." *Optics express* 12.8 (2004): 1622-1631.
[63] Kim, J. T., Park, S., Ju, J. J., Lee, S., & Kim, S. (2010). Low bending loss characteristics of hybrid plasmonic waveguide for flexible optical interconnect. *Optics express*, *18*(23), 24213-24220.
[64] Astley, V., Scheiman, J., Mendis, R., & Mittleman, D. M. (2010). Bending and coupling losses in terahertz wire waveguides. *Optics letters*, *35*(4), 553-555.
[65] Lu, J. T., Hsueh, Y. C., Huang, Y. R., Hwang, Y. J., & Sun, C. K. (2010). Bending loss of terahertz pipe waveguides. *Optics express*, *18*(25), 26332-26338.
[66] D. Marcuse, "Curvature loss formula for optical fibers," *JOSA,* vol. 66, no. 3, pp. 216-220, 1976.
[67] R. T. Schermer and J. H. Cole, "Improved bend loss formula verified for optical fiber by simulation and experiment," *IEEE Journal of Quantum Electronics,* vol. 43, no. 10, pp. 899-909, 2007.
[68] Nallappan, Kathirvel, et al. "Live streaming of uncompressed 4K video using terahertz wireless links." *2018 IEEE International Conference on Communications (ICC)*. IEEE, 2018.
[69] Wang, Cheng, et al. "A 10-Gbit/s wireless communication link using 16-QAM modulation in 140-GHz band." *IEEE Transactions on Microwave Theory and Techniques* 61.7 (2013): 2737-2746.
[70] Nallappan, K., Guerboukha, H., Nerguizian, C. and Skorobogatiy, M., 2018. Live streaming of uncompressed HD and 4K videos using terahertz wireless links. *IEEE Access*, *6*, pp.58030-58042.
[71] Nagatsuma, Tadao, and Kazutoshi Kato. "Photonically-assisted 300-GHz wireless link for real-time 100-Gbit/s transmission." *2014 IEEE MTT-S International Microwave Symposium (IMS2014)*. IEEE, 2014.
[72] Zhou, S. F., Reekie, L., Chan, H. P., Chow, Y. T., Chung, P. S., & Luk, K. M. (2012). Characterization and modeling of Bragg gratings written in polymer fiber for use as filters in the THz region. *Optics express*, *20*(9), 9564-9571.
[73] Yamada, I., Takano, K., Hangyo, M., Saito, M., & Watanabe, W. (2009). Terahertz wire-grid polarizers with micrometer-pitch Al gratings. *Optics letters*, *34*(3), 274-276.
[74] Shin, Young-Min, et al. "Terahertz vacuum electronic circuits fabricated by UV lithographic molding and deep reactive ion etching." *Applied Physics Letters* 95.18 (2009): 181505.
[75] Rossner, T., Sarwar, R., Lyashenko, A., Dörsam, E., & Werthschützky, R. (2013). B3. 4-Hot Stamped Conductors on Nano-Micro Wires Made by Electroplating for Medical Sensors and Micro-Implants. *Proceedings SENSOR 2013*, 248-251.
[76] Lee, Hojoon, and Govind P. Agrawal. "Add-drop multiplexers and interleavers with broad-band chromatic dispersion compensation based on purely phase-sampled fiber gratings." *IEEE Photonics Technology Letters* 16.2 (2004): 635-637.
[77] Simakov, E. I., Heath, C. E., Shchegolkov, D. Y., Kelly, M. J., & Schultz, B. D. (2011, October).

Fabrication and testing of channel-drop filters at millimeter waves. In *2011 International Conference on Infrared, Millimeter, and Terahertz Waves* (pp. 1-3). IEEE.

[78] M. Shalaby, M. Peccianti, Y. Ozturk, M. Clerici, I. Al-Naib, L. Razzari, T. Ozaki, A. Mazhorova, M. Skorobogatiy, R. Morandotti, "Terahertz Faraday rotation in a magnetic liquid: High magneto-optical figure of merit and broadband operation in a ferrofluid," Applied Physics Letters, vol. 100 (24), Article Number: 241107, (2012).

Supplementary Material A: The influence of the accidental degeneracy of the dispersion relations of the SPP mode and bulk modes of a resin cage

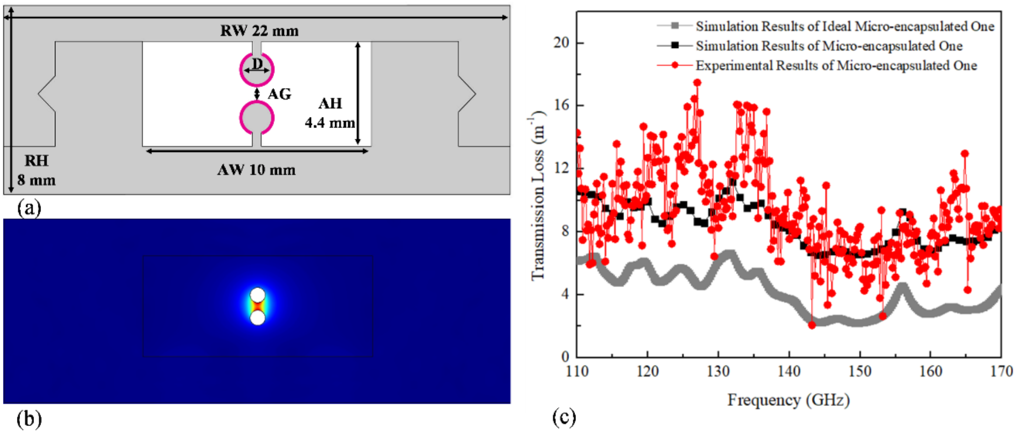

Fig. S1. (a). The schematic of a two-wire waveguide encapsulated by a resin cage featuring wider confined air area than the one indicated in the main-text. (b). The modal electric amplitude field distribution of the supported THz SPP wave at 140 GHz. (c). The modal loss of the THz SPP wave and the measured transmission loss (by amplitude) of the straight two-wire waveguide.

Here we studied a straight two-wire waveguide encapsulated by a resin cage featuring a wider internal dimension than that of the two-wire waveguide indicated in the main-text (see Fig. S1(a)). In these two designs, the geometries of the wire support including wire diameter and inter-wire separation are identical. As larger hollow space is left between the wires and the resin cage in this design, the portion of the supported THz SPP wave distributing in the lossy resin is smaller than that of the waveguide we studied in the main-text (see Fig. S1(b)). Therefore, the computed modal loss and measured transmission loss (by field) of this waveguide are smaller at 140 GHz. However, Fig. S1. (c) shows that the modal loss of the supported THz SPP wave in a broad spectral range 110-135 GHz is larger than that of the other characterized frequencies, and larger measured transmission loss appears in such spectral range in experiments. It is different from the two-wire waveguides indicated in main-text whose measured transmission loss maintains despite of the presence of modal loss peak of the supported THz SPP wave featuring a narrow spectral width in numerical simulations. We believe that the observed modal loss increase is resulting from the hybridization between the THz SPP wave and a mode supported by the resin cage. The spectral position of the resonant frequency is related to the geometry of wires and cage. In this design (Fig. S1. (a)), even with errors in 3D printed structure, the avoiding crossing phenomenon is easy to be excited, thus resulting in the larger transmission loss in a broad spectral range. Therefore, different from the bare two-wire waveguide that features a frequency-insensitive transmission loss, the proposed 3D printed one has to be designed appropriately to avoid the presence of modal loss peaks featuring a large spectral width around the desired operation frequency.

Supplementary Material B: The characterization of the micro-encapsulated two-wire waveguide components and circuits

The proposed 3D printed micro-encapsulated two-wire waveguide components and circuits were studied by using the CW-THz spectroscopy system (TOPTICA Photonics) [1,2]. In such a system (see Figs. S2. (a), S2. (b), S3. (a), S3. (b) and S5. (a)), we mix in a fiber radiation from two distributed feedback (DFB) lasers with slightly different emission wavelengths and combined power of ~30 mW. A 50:50 fiber coupler is used to split the signal into emission and detection arms. The THz radiation is generated in the photomixer (under bias voltage) and corresponds to the beat frequency between the two DFB lasers. A similar photomixer (without bias) and a lock-in amplifier are used to detect the THz radiation. The focused linear-polarized CW-THz beam transmitting through the waveguides is re-collimated and detected. For CW-THz spectroscopy, the THz frequency is scanned by continuously varying the emission wavelengths of the two DFB lasers via adjusting the temperature/current of the Bragg grating in each laser cavity.

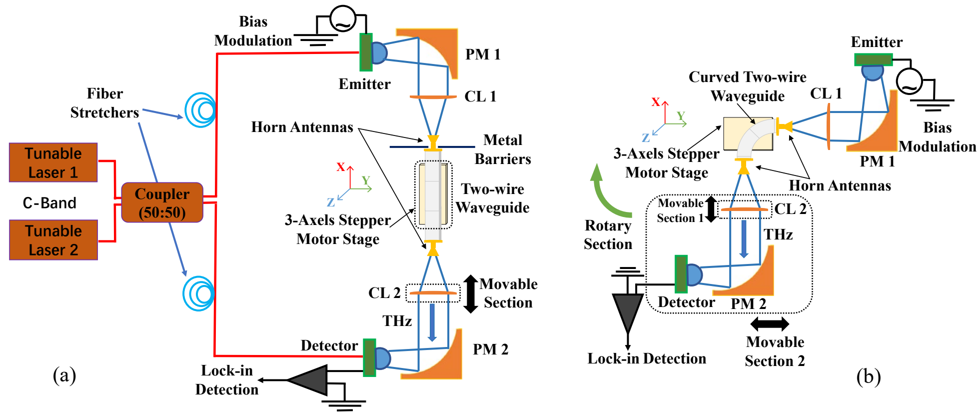

Fig. S2. (a). The experimental setup to measure the propagation loss and the GVD of straight two-wire waveguides, as well as characterize the two-wire waveguide Bragg gratings. PM: parabolic mirror, CL: convex lens. (b). The experimental setup to measure the bending loss of the curved two-wire waveguides.

B.1 The measurement of the propagation loss and GVD of the straight two-wire waveguides and the characterization of the waveguide Bragg gratings (WBGs)

The straight two-wire waveguides were characterized in the following processes. Firstly, the reference spectrum was recorded by placing two united WR6.5 conical horn antennas (Virginia Diode, Inc.) between two neighboring convex lenses CL1 and CL2 with their focal points at the input and output plane of the connected waveguide flanges. Note that CL2 is mounted onto a rail, and represents a movable section (MS) of the spectrometer, thus allowing measuring two-wire waveguides of various lengths, as well as the reference signal. Next, the assembled two-wire waveguide composed of multiple waveguide sections (WSs) was attached with WR6.5 conical horn antennas at its both ends, inserted into the spectrometer with the input and output planes of the waveguide flanges at the focal points of CL1 and CL2 via adjusting the positions of MS and 3-axels stepper motor stage, and then characterized (see Fig. S2. (a)). Finally, by subsequently removing the WSs sandwiched between the two ones connected with the horn antennas and adjusting the position of CL2, the complex transmission spectra (by field) of waveguides featuring different lengths were measured.

In experiments, two sets of waveguide samples were characterized to distinguish the transmission loss α_{st} and the coupling loss Cl between neighboring WSs. Each set includes a same amount of WSs with the same length l. By comparing the measurements with the reference, the normalized transmittance (by power) of waveguides can be given as follow:

$$T_{ml} = C_{\text{in}} C_{\text{out}} Cl^{m-1} \cdot \exp\left(-2\alpha_{\text{st}} ml\right) \quad [S1]$$

In which, C_{in} and C_{out} refer the power coupling coefficient between the two-wire waveguides and WR6.5 waveguide flange that is assumed as a fixed constant, while m refers the amounts of the measured WSs. By expressing the Eq. [S1] as the logarithms of e and comparing the transmittance of two waveguides integrated by the same amount of sections from different sets of samples, the transmission loss α_{st} was derived by the following equation,

$$\log(T_{ml_1})\text{-}\log(T_{ml_2})\text{=-}2m\alpha(l_1-l_2) \quad [S2]$$

Afterwards, with the measured transmission loss α_{st}, the average coupling loss *Cl* was obtained by comparing the transmittance of waveguides exhibiting different lengths.

The phase measurement was performed by the CW-THz spectroscopy using an optical delay line in the form of polarization-maintaining fiber wound piezoelectric elements. The effective RI of the two-wire waveguide was then retrieved from the phase of normalized transmission spectrum (by field) that has been obtained by dividing the measured complex transmission spectrum of the waveguides by the reference one [3]. Afterwards, the effective RI was fitted into a two-order polynomial of angular frequency ω to mitigate the influence of noise on the measured raw data. The GVD was finally computed as the second derivative of the derived waveguide propagation constant with respect to the angular frequency ω by Eq. [3].

To characterize the two-wire waveguide Bragg gratings, a 3D printed two-wire waveguide with slits (the schematic diagram is shown in Fig. 4. (a)) was placed with its two ends at the focal points of the CL1 and CL2. The reference transmission spectrum (by field) was obtained by measuring the waveguide without paper at first. After inserting the paper-based periodic metalized structure between wires, the transmission spectra (by field) of WBGs were recorded. The transmittances were obtained by dividing them by the reference one.

B.2 The measurement of the bending loss of the two-wire waveguide bends

The transmission spectra of the two-wire waveguide bends were measured by the following process. In order to avoid the difference in the coupling coefficient between WR6.5 waveguide flange and waveguides with different bend radiuses, each characterized curved waveguide is in the form of a bend section featuring bending radian of 90° terminated with two straight sections with the same length of 5 mm. Firstly, the reference spectrum was obtained by characterizing a straight waveguide featuring the same length with the curved one. The measurement was conducted via the experimental setup shown in Fig. S2. (b) after clockwise rotating the rotary section by

90°. In the next step, we reset the rotary section and placed the curved two-wire waveguide with the input plane of its connected waveguide flange at the same position with the one of the straight waveguide. Finally, we placed the CL2 with its focal point at the output plane of the other waveguide flange connected with the curved two-wire waveguide by finely adjusting the MS1 and MS2 positions on X and Y axials before measurement.

In experiments, the transmission spectra of curved two-wire waveguides with the axis of rotation parallel to the line connecting wire centers were measured at first. In order to characterize the curved two-wire waveguides with the axis of rotation perpendicular to the line connecting wire centers, we rotate the THz emitter and receiver by 90° to keep the polarization direction of the transmitting linear polarized THz beam parallel to the line connecting wires of characterized waveguides. Afterwards, the transmission spectra can be measured by using the same experimental setup shown in Fig. S2. (b).

In order to derive the bending loss α_b from the experimental results, the power coupling coefficient $C_{st\text{-}be}$ between straight and bent waveguide was computed using mode matching method theoretically (the results are shown in Fig. 3. (e)) [4]. Additionally, given the high similarity in the modal field distribution of the THz SPP wave supported by the bent and straight waveguides (see Figs. 1. (d), 3. (a), and 3. (b)), the power coupling coefficient between two bent WSs is assumed identical to the one between two straight WSs. Thus the bending loss α_b of waveguide bends can be extracted by comparing the measured transmission spectrum of the bend with that of the corresponding straight waveguides by,

$$2\alpha_{\mathrm{b}} = -\log\left(T_{\mathrm{curve}} / T_{straight} / C^{2}{}_{st-be}\right) / (0.5\pi R) \qquad \text{[S3]}$$

In which, the R refers the bend radius of the waveguide bends, T_{curve} and $T_{straight}$ refer the transmittance (by power) of the curved and straight waveguides.

Supplementary Material C: The characterization of two-wire waveguide-based THz coupler

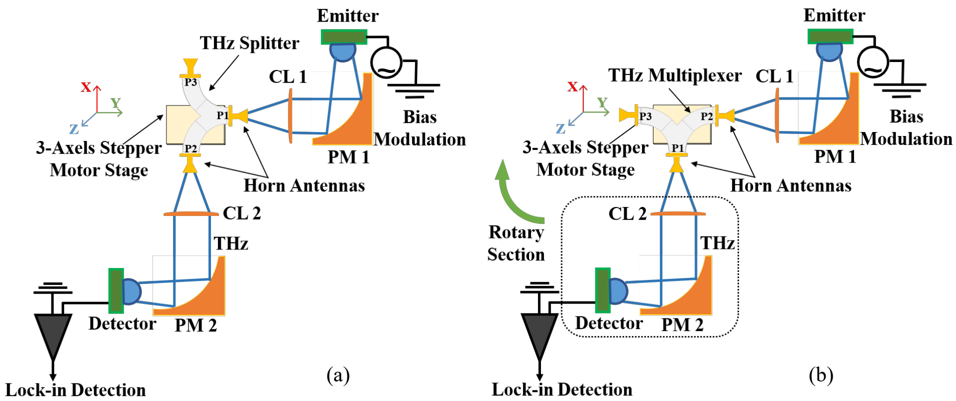

Fig. S3. (a). The experimental setup to characterize the THz splitter. (b) The experimental setup to characterize the THz multiplexer.

The two-wire waveguide-based THz coupler was characterized by the following processes. Firstly, each port of the THz coupler was connected with a WR6.5 conical horn antenna containing a waveguide flange. When serving as a THz splitter, the coupler was inserted into the CW-THz spectrometer system with the input and output planes of waveguide flanges connected with ports 1 and 2 at the focal points of CL1 and CL2 (see Fig. S3. (a)). The transmission spectrum received at the output port 2 was recorded when the THz light was launched into the port 1. Then, the THz splitter was turned over to measure the transmission spectrum of the output port 3. When serving as a THz multiplexer, the coupler was placed with the input and output planes of waveguide flanges connected with ports 2 and 1 at the focal points of CL1 and CL2 (see Fig. S3. (b)). The transmission spectrum received at the output port 1 was recorded when the THz light was launched into the port 2. Then, we clockwise rotated the rotary section by 90°, and measured the transmission spectrum of the output port 3. Afterwards, the THz coupler was replaced by a straight waveguide connected with WR6.5 conical horn antennas at its both ends (see Fig. S3. (b)). The transmission spectrum of the straight waveguide was measured with the same incident THz light (The measurement process is detailed in Supplementary Material B.1). The reference spectrum was derived from this transmission spectrum by,

$$T_{\mathrm{ref}} = T_{\mathrm{straight}} / \exp(-2\alpha_{\mathrm{st}} l_{straight}) / Cl \quad [S4]$$

Additionally, the transmission spectrum of a two-wire waveguide bend featuring the same geometry of half of a THz coupler (see Fig. 3. (b)) was choose as a control of that of the THz coupler. The transmission spectrum of the waveguide bend was measured with the same THz light is launched into it via a WR6.5 conical horn antenna (the detailed process is indicated in supplementary material B.2).

Supplementary Material D: The theoretical analysis of a two-wire WBG

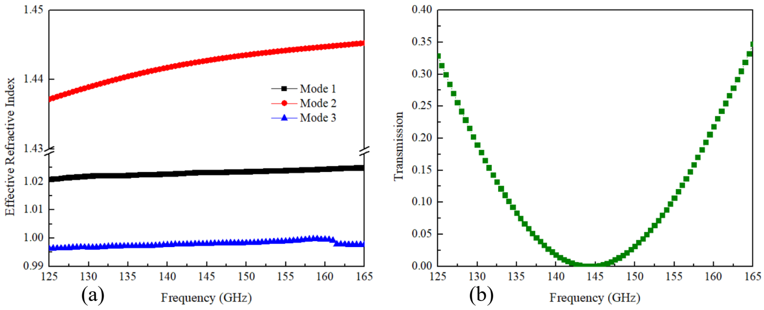

Fig. S4. (a) The effective refractive index of the Modes 1, 2 and 3. (b) The theoretical results of the transmission of a WBG containing a single period featuring a pith of 1.5 mm and a metalized section width of 0.7 mm.

In this section, we theoretically study the two-wire WBG that is demonstrated in Section 3.3 of the main-text. The pitch and the width of the metalized section in one period are 1.5 mm and 0.7 mm, respectively. Around the desired operation frequency of 140 GHz, the power coupling coefficient between Modes 1 and 3 (δ) is computed as 0.86 by mode matching method [4]. Additionally, Fig. S4. (a) shows the effective RIs of the Modes 1, 2, and 3 that are obtained by using mode analysis to study the cross-sections of the Sections 1 and 2 (see Fig. 4. (b)) using COMSOL Multiphysics. Assuming these modes are lossless, and therefore taking the real part of their effective RIs into Eq. [6], Fig. S4. (b) shows the transmission of THz light through one period of WBG. The spectral position of the transmission dip is at 144 GHz, which agrees well with the numerical and experimental results that are demonstrated in main-text.

Supplementary Material E: The characterization of two-wire waveguide-based Add-Drop Multiplexer (ADM)

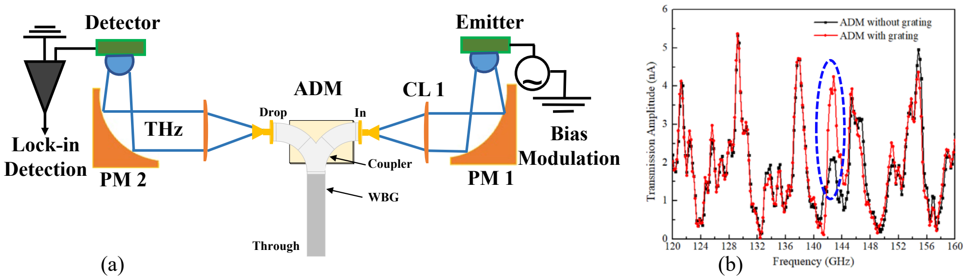

Fig. S5. (a). The experimental setup to characterize the THz ADM. (b) Transmission amplitude of the ADM with and without paper-based metalized periodic pattern inserted into the integrated WBG.

The ADM was characterized by taking the following process. Firstly, the THz coupler and WBG were assembled using the interconnects at the end facets of both waveguide components, and two WR6.5 conical horn antennas containing waveguide flanges were connected with the In and Drop ports. Afterwards, the ADM was inserted into the CW-THz spectrometer system with the input and output planes of waveguide flanges connected with In and Drop ports at the focal points of CL1 and CL2 (see Fig. S5. (a)). Finally, when the THz light was launched into the port 1, the transmission spectra received at the Drop port with and without paper-based metalized periodic structure inserted into the WBG were recorded (see Fig. S5. (b)).

In order to reduce the noise caused by the coupling between two curved arms around the Y-shaped intersection, the difference between these two transmission spectra (see the blue dotted region in Fig. S5. (b)) is shown in Fig. 6. (c), from which a transmission peak can be distinguished around the Bragg frequency of the integrated WBG.

Reference

[1] A. Roggenbuck, H. Schmitz, A. Deninger, I. C. Mayorga, J. Hemberger, R. Güsten, and M. Grüninger, “Coherent broadband continuous-wave terahertz spectroscopy on solid-state samples,” New J. Phys. 12(4), 043017 (2010).

[2] D. Stanze, A. Deninger, A. Roggenbuck, S. Schindler, M. Schlak, and B. Sartorius, “Compact CW terahertz spectrometer pumped at 1.5 μm wavelength,” J. Infrared Millim. Terahertz Waves 32(2), 225–232 (2011).

[3] H. Guerboukha, K. Nallappan, and M. Skorobogatiy, “Toward real-time terahertz imaging,” Adv. Opt. Photonics 10(4), 843–938 (2018).

[4] Skorobogatiy, M., 2012. Nanostructured and Subwavelength Waveguides: fundamentals and applications. John Wiley & Sons. (Ch. 2.6)